DOI: https://doi.org/ 10.25100/iyc.v20i1. 6040 MATERIALS ENGINEERING AND COMPUTATIONAL SIMULATION

DFT computational study of the tetragonal (P4/nmm) WO_3 (001) Surface

INGENIERIA DE MATERIALES Y SIMULACION COMPUTACIONAL

Estudio computacional por DFT de la superficie (001) de WO_3 tetragonal (P4/nmm)

Álvaro Loaiza-Orduz[1], Eduard Araujo-López[1], Julian D. Urresta[1] ,Mario Llano-Restrepo[2§]

[1]Facultad de Ciencias Naturales y Exactas, Departamento de Química, Universidad del Valle. Cali, Colombia.
[2]Facultad de Ingeniería, Escuela de Ingeniería Química, Universidad del Valle. Cali, Colombia
alvaro.loaiza@correounivalle.edu.co, jesus.araujo@correounivalle.edu.co,
julian.urresta@correounivalle.edu.co, [§]mario.llano@correounivalle.edu.co

(Recibido: Mayo 05 de 2017 - Aceptado: Agosto 14 de 2017)

Abstract

Tetragonal WO_3 is important for catalytic reactions such as the hydration of ethylene, which is an alternative choice to ethanol production by fermentation. However, very little is known about the structural and electronic properties of the tetragonal WO_3 surfaces with possible catalytic activity. In this work, the WO_3 (001) surface was characterized by means of density-functional-theory computer simulations. The crystal unit cell parameters and the corresponding angles and bond distances were determined, and the density of states (DOS) for the bulk was calculated. The band gap turned out to be 0.6 eV. Two (001) surface models were generated, one without oxygen atoms at the surface (model I) and the other with only one oxygen atom at the surface (model II). For both models, four converged layers of atoms and a vacuum of 14 Å between neighboring slabs were used for the calculations. Values of 135.01 and 40.55 meV/ Å^2 for the surface energies of models I and II, respectively, were obtained, showing that model II is more likely to represent the WO_3 catalyst. The density of states (DOS) was calculated for each surface model, and both of them exhibited an energy gap close to zero.

Keywords: *DFT, DOS, (001) surface, structural optimization, tetragonal WO_3.*

Resumen

El WO_3 tetragonal tiene importancia en reacciones catalíticas tales como la hidratación del etileno, que es una alternativa a la obtención de etanol por fermentación. Sin embargo, muy poco se conoce acerca de la estructura y propiedades electrónicas de la superficie de WO_3 tetragonal con posible actividad catalítica. En este trabajo, se caracterizó la superficie WO_3 (001) mediante simulaciones computacionales utilizando la teoría del funcional de densidad. Se determinaron los parámetros de la celda unitaria y los correspondientes ángulos y distancias de enlace, y se calculó la densidad de estados (DOS) en volumen obteniéndose un valor para el ancho de banda de 0.6 eV. Se generaron dos modelos de superficie en la dirección (001) del volumen, uno sin átomos de oxígeno en la superficie (modelo I) y otro con un solo átomo de oxígeno en la superficie (modelo II). Para ambos modelos se usaron en los cálculos cuatro capas de átomos y un vacío de 14 Å entre losas vecinas. Se obtuvieron valores de 135.01 y 40.55 meV/ Å^2 para las energías superficiales de los modelos I y II respectivamente, mostrando que el modelo II tiene asociada una mayor probabilidad de representar al catalizador de WO_3. Se calculó la densidad de estados de ambos modelos, observándose un ancho de banda cercano a cero.

Palabras clave: *DFT, DOS, optimización estructural, superficie (001), WO_3 tetragonal.*

1. Introduction

The study of catalytic reactions is motivated by their many industrial applications. In particular, the transformation of raw materials into fuels or highly demanded precursors is currently drawing much attention. The conversion of syngas to ethanol (1) and the hydration of ethylene to ethanol (2-9) stand out among the catalytic reactions of increasing industrial interest (10). Ethanol has become a highly demanded product, presently being obtained mostly from fermentation processes (11, 12), which require a careful implementation and control. However, for almost 70 years, the direct catalytic hydration of ethylene has been the alternative choice to obtain ethanol in the petrochemical industry (13-16).

The main disadvantage of the petrochemical route is that the yield and selectivity of the hydration reaction depend strongly on the kind of solid catalyst used to carry out the reaction, so that the performance of some catalysts can turn out to be economically unfavorable. The capability to improve the economics of the hydration process depends on the knowledge of the microscopic variables that determine the performance of the catalysts. As a complement to the experimental methods, it is advisable to perform computer simulation studies of the catalysts, with the aim of exploring and understanding the fundamental phenomena that occur on a catalyst at the nanometric scale.

By means of the wet impregnation method (17-19), Salazar (20) synthesized two types of tungsten-based catalysts, one using titania (TiO_2) as the support of the active phase and the other using zirconia (ZrO_2). The catalyst with WO_3 (active phase) supported on TiO_2 (rutile) showed higher activity and selectivity toward ethanol production.

The tetragonal phase has been reported as the most common crystalline form of WO_3 existing at the operating conditions used for the calcination stage that is performed after the wet impregnation of the catalyst. Such a tetragonal phase can be present in two kinds of symmetries (21): *P*4/*ncc* (at 1173.15 K) and *P*4/*nmm* (at 1443.15 K).

From the consideration of the computational cost, it is more convenient to perform simulations with the *P*4/*nmm* crystal because it has a primitive cell with 8 atoms (W_2O_6) whereas the *P*4/*ncc* crystal has a cell with 16 atoms (W_4O_{12}). Therefore, for the present work, the experimental data reported by Locherer et al. (21) for the *P*4/*nmm* crystal were chosen as the starting point for the computation of the structure of the WO_3 unit cell.

With regard to previous studies of the ethylene hydration reaction using computational catalysis, two works can be mentioned. Nakagawa *et al*. (22) performed DFT-B3LYP calculations with Gaussian orbitals to study two reaction paths for the ethylene hydration catalyzed by metal cations and oxoacids. Van Erp & Meijer (23) used the Carr-Parinello approach to study the hydration of ethylene in protonated water clusters.

The present work was focused on the active phase of WO_3. After the optimum values of the computational parameters that are required to carry out accurate density-functional-theory (DFT) calculations in a periodic system of the tetragonal *P*4/*nmm* WO_3 crystal were defined, the structure of the catalyst was studied by determining its electronic and energetic characteristics.

To date, no works have yet been published on the hydration of ethylene over WO_3 surfaces by means of DFT periodic calculations.

2. Methodology

2.1. Computational details

The Quantum Espresso (QE) package (24, 25) was used to perform all the spin-polarized DFT calculations in the generalized-gradient approximation (GGA) with the Perdew-Burke and Ernzerhof (PBE) (26) exchange and correlation functional and the van der Waals dispersion forces (vdW) (27). A plane wave expansion was used to represent the electronic states of the valence electrons and Vanderbilt ultra-soft pseudopotentials were used to represent the interactions of the valence electrons with the ions. The k-point grid was generated through the Monkhorst & Pack method (28). All the crystalline structures were generated using the XCrysDen program (29).

2.2. Convergence study of the simulation parameters

In ideal DFT periodic calculations for crystalline solids, it is desirable to use the largest possible

k-points grid and also high values for the kinetic energy cutoff for the wave-functions (E_{cut}) and the kinetic energy cutoff for the charge density and potential (E_{cutrho}), with the aim of representing the system in the most realistic way possible. Nevertheless, given the time constraints of simulation research works and the computational limitations of the current numerical processors, a balance should be found between the quality of the results and the efficiency of the calculations. This is the motivation for a parameter convergence study, which seeks to reduce the relative error of the results by calculating the energy differences between two crystalline phases of the solid as a function of a specific parameter.

In this work, the energy differences between the tetragonal *P*4/*nmm* and the simple cubic phases of WO_3 were calculated. The E_{cut} value was started at 5 Ry and increased by 5 Ry at each step up to a maximum value of 120 Ry. E_{cutrho} values of 8, 10, and 12 times the value of E_{cut} were tried. The number of k-points for the x axis (k_x) was varied between 2 and 10, with successive increments of 2, and the number of k-points for the y and z axes (k_y and k_z) were obtained from k_x, depending on the conventional crystal size.

If the lattice parameters of a unit cell obey the constraints $a=b<c$ where $c=2a$, then the number of k-points for the *x*, *y*, and *z* axes can be written as k_x, k_x, and $k_x/2$, respectively. Otherwise, if the parameters obey the constraints $a=c<b$ where $b=2a$, then the number of k-points can be written as k_x, $k_x/2$, and k_x, respectively.

The optimal values of the parameters were found by means of an iterative process in which the parameter values that were obtained at the end of the first convergence test were used as the starting values for the second convergence test, and the values obtained from that second test were used as the starting values for the third test, and so on until the parameters reached stable values.

The iterative process used to obtain the optimal values of the parameters is comprised of the following steps:

Step 1. The value of E_{cut} is varied until convergence is achieved while using the values of E_{cutrho} and k_x that were obtained in the previous cycle. For the first cycle, the starting values of E_{cutrho} and k_x are 10 and 2, respectively, and k_y and k_z are defined by following the rules explained above.

Step 2. The value of E_{cutrho} is varied until convergence is achieved by keeping unchanged the value of k_x that was obtained from the previous cycle and using the value of E_{cut} obtained from step 1.

Step 3.The value of k_x is varied until convergence is achieved while using the values of E_{cut} and E_{cutrho} obtained from steps 1 and 2, respectively.

Step 4. The values of E_{cut}, E_{cutrho}, and k_x obtained from steps 1 to 3 are compared with the values obtained at the end of the previous cycle. If the two sets of values are in disagreement, another iterative cycle (steps 1 to 3) is started. If the two sets of values are in agreement, the iterative process is terminated.

A similar parameter optimization method has previously been implemented by one of the authors of the present work (30). For WO_3 (tetragonal *P*4/*nmm*), the optimization of the parameters required two iterative cycles and the corresponding results are given in Table 1.

Table 1. *Values of the converged parameters.*

WO_3 (first iteration)			WO_3 (second iteration)		
E_{cut} (Ry)	E_{cutrho}/E_{cut}	n_k	E_{cut} (Ry)	E_{cutrho}/E_{cut}	n_k
50	10	8	50	10	*

** A second iteration of the number of k-points was not required because the values of E_{cut} and E_{cutrho} had already converged.*

The optimal values of the parameters are as follows: E_{cut} = 50 Ry, E_{cutrho} = 10 E_{cut} and n_k = 8. These values were used in all subsequent calculations for the tetragonal phase of WO_3.

2.3. Surface energy

The surface energy, E_{surf}, was calculated from the following expression (31-35):

$$E_{surf} = \frac{1}{2A}\left\{E_{slab} - \left[E_{bulk}\left(\frac{n_{slab}}{n_{bulk}}\right) \pm \sum_{i=1}^{M} \Delta N_i E_i\right]\right\} \quad (1)$$

where A is the area of the slab perpendicular to the z axis, E_{slab} is the total energy of the slab, E_{bulk} is the energy of the structure as a bulk, n_{slab} is the number of formula units of the slab and n_{bulk} is the number of formula units in the bulk. When the structure is stoichiometric, there is no loss or gain of energy by removing or adding atoms to the slab; in consequence, the summation term $\pm \sum_{i=1}^{M} \Delta N_i E_i$ is equal to zero and Eq.(1) simplifies to the first two terms. If the structure is not stoichiometric, it is necessary to take the summation term into account, where ΔN_i stands for the number of atoms being removed from or added to the slab and E_i is calculated from the following expression:

$$E_i = \frac{1}{x}\left(E_{i_x} + \Delta\mu_{i_x}\right) \quad (2)$$

Where Ei_x and $\Delta\mu i_x$ are the total energy and the chemical potential change of molecular species i_x, and x is the number of atoms of element i in species i_x.

3. Results and discussion

3.1. Tetragonal (*P4/nmm*) WO_3 bulk

Based on the optimal values of the parameters, a full relaxation of the tetragonal P4/nmm WO_3 unit cell was performed. All atomic positions and lattice parameters of WO_3 were relaxed by using the variable-cell command of the QE package. The starting values of the lattice parameters and atomic coordinates were taken from the study by Locherer *et al*. (21).

The WO_3 structure has three different W-O bonds, designated as W-O1, W-O2 y W-O3. Also, two angles, designated as θ and ϕ, are required to describe the structure's geometry. The results obtained in this work agree with those reported in the open literature (see Table 2 and Figure 1).

Table 2. *Lattice parameters, bond distances and angles of the tetragonal (P4/nmm) WO_3 bulk.*

Variable	***a,b*** (Å)	***c*** **(Å)**	**W-O1 (Å)**	**W-O2 (Å)**	**W-O3(Å)**	**θ (º)**	**ϕ(º)**
Locherer *et al.* (21)	5.294	3.928	1.8899	2.2015	1.7269	82.067	97.933
Chatten *et al.* (35)	–	–	1.897	2.336	1.73	–	–
This work	5.322	3.918	1.8989	2.1566	1.7612	82.238	97.762
ε_r(%)*	0.526	0.255	0.474	2.082	1.948	0.208	0.175

** Relative percentage error between the experimental values reported in (21) and the results of this work.*

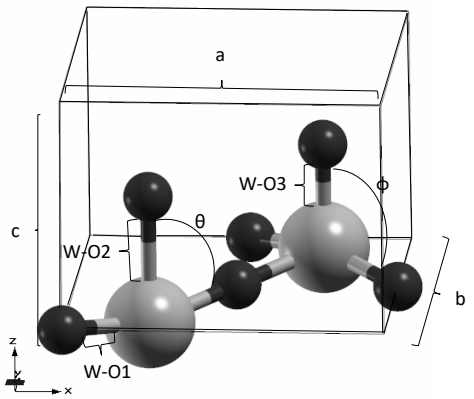

Figure 1. *Tetragonal P4/nmm bulk. The oxygen atoms are in red, the tungsten atoms are in gray.*

3.2 Density of states and band gap of the *P4/nmm* WO_3 bulk

A density of states (DOS) calculation for the bulk was performed by taking into account the geometry described in Section 3.1. Figure 2 shows that the 2*p* states of the oxygen atoms are predominant in the valence band and the 5d states of the tungsten atoms are predominant in the conduction band.

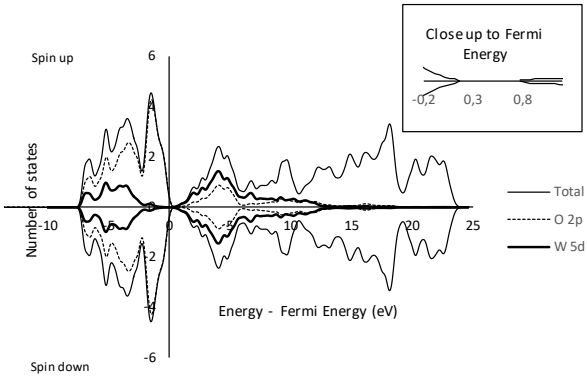

Figure 2. *Density of states (DOS) of tetragonal P4/nmm* WO_3.

The band gap value obtained in this work is similar to the values reported in other theoretical studies (see Table 3). As far as the authors' knowledge is concerned, no experimental values have been reported for the band gap of tetragonal *P*4/*nmm* WO_3. However, Wang *et al*. (36) suggested that the band gap of the tetragonal phase should be similar to that of the cubic phase because the tetragonal phase is just a deformation of the cubic phase. Indeed, several computational methodologies applied to these phases yield similar results (36). Even so, the band gap of 2.6 eV reported by Hjelm *et al.* (37) for the cubic phase is quite different from the values listed in Table 3 for the tetragonal phase. Such discrepancies are common in DFT studies for solids and are related to the fundamental aspects of the theory at the physical interpretation of the bands and orbitals (38). A possible way of elucidating such discrepancies is by implementing a specific hybrid functional to emulate the band gap (39). In this work, the widely used functional known as PBE was chosen because it has been already optimized using ultrasoft pseudopotentials, which ensures the reliability of the geometry and energy calculations.

Table 3. *Band gap values for the bulk as obtained in this work and other theoretical studies.*

	XC Functional	WO_3 phase	Band gap (eV)
This work	sp*-PP-PBE+vdW	Tetragonal *P*4/*nmm*	0.6
Chatten *et al.* (35)	PP**-RPBE	Tetragonal *P*4/*nmm*	0.66
Wang *et al*. (36)	B3LYP	Tetragonal *P*4/*nmm*	1.85
Alvarez-Quiceno et al. (40)	PP-PBEsol	Tetragonal *P*4/*nmm*	0.97

*Spin polarized ** Ultrasoft pseudopotential

3.3 Tetragonal *P4/nmm* (001) surfaces

The plane (001) is most frequently mentioned in the work by Salazar (20). The (001) surface is equivalent to the WO_3 bulk with a vacuum space in the *z* axis.

In Figure 1, there are two protruding oxygen atoms; this could be a problem during the adsorption of electronegative molecules such as water and ethylene (the reactants for the production of ethanol) due to the electrostatic repulsion between negative point charges (41, 42). Also, it is convenient to work with structures without dipoles because these can be troublesome for the calculations (43).

From these considerations, two surface models are proposed. Model I has no protruding oxygen atoms on the surface but it is not stoichiometric with regard to the WO_3 unit. Model II has the same number of oxygen atoms at both sides of the surface and it is stoichiometric with regard to the WO_3 unit. The layers are defined for each model as shown in Figure 3.

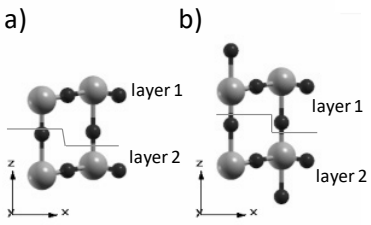

Figure 3. *Models proposed for the (001) surface of the tetragonal P4/nmm* WO_3 *a) Model I. Non-stoichiometric and non-dipole structure b) Model II. Stoichiometric and non-dipole structure.*

A proposal similar to model II has been reported for the monoclinic WO_3 (001) surface by taking into account superficial reconstructions of experimental works (44).

3.4. Surface energy expressions for the tetragonal *P*4/*nmm* WO_3 (001) surface

Suitable values for both the number of layers and the vacuum distance between the slabs have to be chosen in order to represent the nanostructures with a modest computational cost and achieve an appropriate model of the surface.

By following a procedure similar to the parameter convergence tests for the bulk described in Section 2.2, the optimum number of layers and the vacuum distance between the slabs were found by searching for the values of those parameters that turn out to be associated to consecutive calculations with a surface energy difference less than a prescribed tolerance. In this work, we used a tolerance of 0.5 meV/Å^2, which looks much lower than the one used in similar works (44, 45).

In contrast to the parameter convergence tests for the bulk (in which total energies are involved), the convergence of the surface model is determined from the computation of surface energies.

As model I can be obtained from model II by removing two oxygen atoms (one atom at each end of the slab, see Figure 3), the summation term for model I is not null and the energy for model I should be larger than the energy for model II. Therefore, for model I, Eq.(1) takes the following form:

$$E_{surf} = \frac{1}{2A}\left[E_{slab} - E_{bulk}\left(\frac{n_{slab}}{n_{bulk}}\right) + \Delta N_0 E_0\right] \quad (3)$$

For a convenient calculation of E_0, the easiest choice for the molecular species i_x in Eq.(2) is the molecular oxygen (triplet) O_2. In that way, Eq.(2) takes the following form:

$$E_o = \frac{1}{2}\left(E_{O_2} + \Delta\mu_{O_2}\right) \quad (4)$$

Where the chemical potential change $\Delta\mu O_2$ is given by the expression

$$\Delta\mu_{O_2} = \mu_{O_2}{}^o - RTln\left(a_{O_2}\right) \quad (5)$$

In Eq.(5), R is the universal gas constant, T is the absolute temperature, a_{O2} is the activity of O_2, and $\mu_{O2}{}^o$ is the standard chemical potential of the oxygen molecule and is given by the following expression (46):

$$\mu_{O_2}{}^o = \frac{G_{O_2}{}^o}{n} = \frac{H_{O_2}{}^o}{n} - T\frac{S_{O_2}{}^o}{n} \quad (6)$$

Where n stands for the number of oxygen molecules, and $G^0_{O_2}, H^0_{O_2}$ and $S^0_{O_2}$ are the standard Gibbs free energy, enthalpy and entropy of formation of the oxygen molecule, respectively, which by definition are set to zero, because the triplet oxygen is the most stable structure relative to the oxygen atom. Besides, as the system is calculated purely from DFT, the absolute temperature is equal to 0 K. In this way, from Eqs. (5) and (6), it follows that $\Delta\mu_{O2} = 0$.

Taking all of the above into account and the fact that $\Delta N_o = 2$ because two oxygen atoms are removed when the molecular species is O_2, the surface energy of model I is given by

$$E_{surf} = \frac{1}{2A}\left[E_{slab} - E_{bulk}\left(\frac{n_{slab}}{n_{bulk}}\right) + E_{O_2}\right] \quad (7)$$

The summation term in Eq.(1) vanishes for model II because this is stoichiometric. Therefore, for model II, Eq.(1) takes the following form:

$$E_{surf} = \frac{1}{2A}\left[E_{slab} - E_{bulk}\left(\frac{n_{slab}}{n_{bulk}}\right)\right] \quad (8)$$

3.5. Layer and vacuum convergence for the tetragonal P4/*nmm* (001) WO_3 surface

The procedure used to obtain the number of layers and the vacuum distance between the slabs can be summarized as follows. Firstly, the number of layers was converged using an arbitrary vacuum distance (16 Å), i.e., the number of layers was successively increased until the surface energy E_{surf}

did not change more than a prescribed tolerance of 0.5 meV/Å^2. By using the resulting number of layers, the vacuum distance was changed until the surface energy did not change more than the same prescribed tolerance. This procedure differs from the one previously used for the parameter convergent tests because it is not iterative. These kinds of calculations are computationally more costly, and the assumption is made that changes will not occur in a second iteration because as shown in Figure 4b, no significant changes occur by varying the vacuum distance.

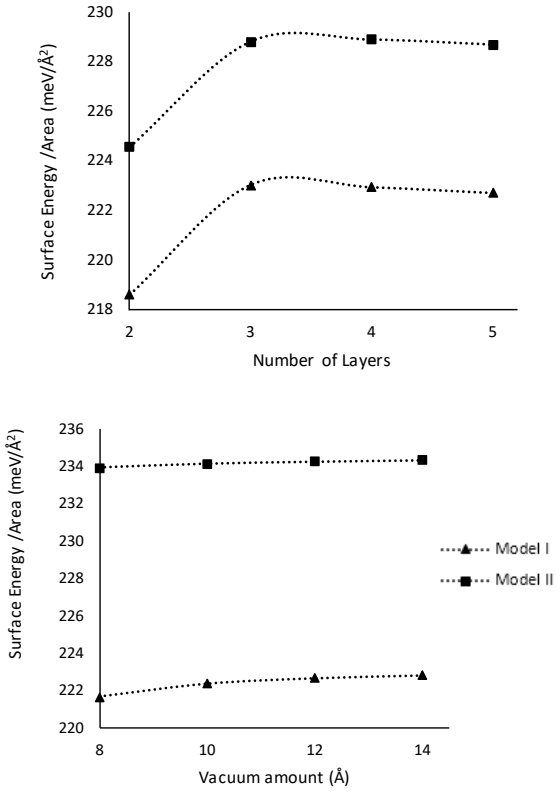

Figure 4. *a) Surface energy as a function of the number of layers and b) surface energy as a function of the vacuum distance between slabs for the tetragonal P4/nmm (001) WO_3 surface.*

Both models of WO_3 can be represented accurately by four layers and at least 10 Å of vacuum. However, in order to avoid the self-interaction between periodic slabs, a final value of 14 Å was chosen for all subsequent calculations.

3.6. Relaxation of the tetragonal *P*4/*nmm* WO_3 (001) surface

A full relaxation of only the atoms inside the slabs was performed for both models by using the values of the number of layers and vacuum distance found previously. This relaxation process is similar to the relaxation of the bulk (*vc-relax*), except for the avoidance of supercell movements.

As shown in Figure 5, the structural changes of both models due to such a relaxation are quite drastic. The surface model I turned into a tungsten coplanar structure with respect to the z axis (W1-W2, W3-W4, etc.). On the other hand, in the relaxed surface model II each column with a WO end is pulling along its length.

With regard to the bond distances (Table 4), surface model I has symmetric W-O bonds along the z axis, and surface model II simultaneously exhibits very short and long bonds. That model II changes more than model I by relaxation follows from the fact that the sum of the absolute values of the bond length differences before and after relaxation of model II is about three times the corresponding sum for model I.

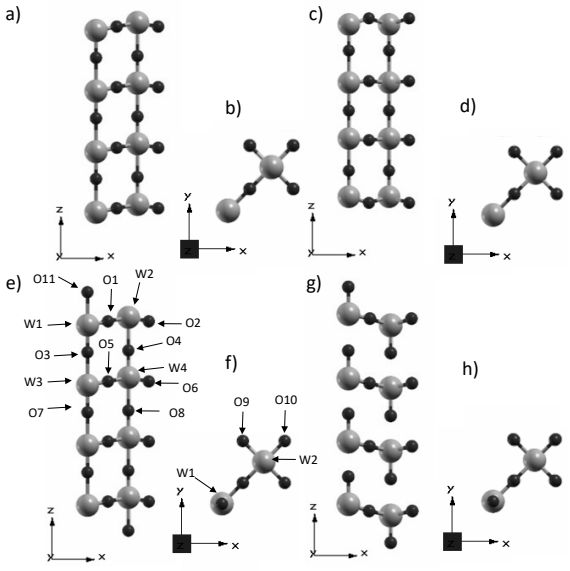

Figure 5. *Views of the tetragonal P4/nmm WO3 (001) surface: (a, b) and (e, f) model I and model II before optimzation, respectively. (c, d) and (g, h) model I and model II after optimization, respectively.*

Table 4. *Tungsten-oxygen bond lengths before and after structural relaxation.*

	Before relaxation		After relaxation	
Bond	**Model I**	**Model II**	**Model I**	**Model II**
W1-O1(Å)	1.8989		1.9248	1.9384
W1-O3(Å)	1.7612		1.7347	2.3067
W1-O11(Å)	-	2.1566	–	1.7061
W2-O1(Å)	1.8989		1.9248	1.8943
W2-O2(Å)	1.8989		1.9248	1.8943
W2-O4(Å)	2.1566		1.7347	1.7353
W2-O9(Å)	1.8989		1.9248	1.8943
W2-O10(Å)	1.8989		1.9248	1.8943
W3-O3(Å)	2.1566		2.1331	1.7537
W3-O5(Å)	1.8989		1.8843	1.9058
W3-O7(Å)	1.7612		1.8644	2.2148
W4-O4(Å)	1.7612		2.1331	2.2042
W4-O5(Å)	1.8989		1.8843	1.9034
W4-O6(Å)	1.8989		1.8843	1.9034
W4-O8(Å)	2.1566		1.8644	1.7506

3.7. Surface energy of the tetragonal *P*4/*nmm* WO_3 (001) surface

The relaxation or geometry optimization of the surface models not only yields a change of structure but also a change of surface energy, which decreases for both models, and the larger decrease occurs for model II.

The decrease in surface energy is related with the stability of the slab and the rearrangement of the superficial atoms, mainly. This result is as expected: more stability in exchange with geometrical distortions.

The relaxed surface model II turns out to be energetically more favorable than the relaxed surface model I because all the tungsten atoms in model I are penta-coordinated (instead of hexa-coordinated as in the bulk), and in consequence, surface model I has a larger energy.

Model II turns out to be more suitable to represent the WO_3 catalyst because of its lower surface energy and correspondingly greater stability. This model has a surface energy comparable to that of the same plane of the monoclinic phase of WO_3 (Table 5). Despite being different crystalline phases, the monoclinic (001) surface is similar to surface model II of the tetragonal phase. To date, no other works have been published to report the energy of a WO_3 surface without protuberant oxygen atoms. This could be due to the additional difficulty involved in the implementation of the mathematical expression, Eq. (1), for the calculation of the surface energy of non-stoichiometric slabs.

Table 5. *Surface energy of the WO_3 (001) surfaces.*

	XC Functional	WO_3 surface	E_{surf} (meV/Å^2)
This work	sp-PP-PBE+vdW	Tetragonal *P*4/*nmm* (001) - Model I	135.01 (222.96)*
	sp-PP-PBE+vdW	Tetragonal *P*4/*nmm* (001) - Model II	40.55 (228.92)*
Wang *et al.* (36)**	PP-PW91	ε-Monoclinic (001)	20.6

* Slab before relaxation.

** Calculated with six free layers.

3.8 Projected density of states and band gap of the tetragonal *P*4/*nmm* WO_3 (001) surface

Figure 6 shows the projected density of states (PDOS) of the tetragonal WO_3 surfaces. As in the bulk, in surface models I and II the presence of 2*p* states for the oxygen atoms in the valence band and 5*d* states for the tungsten atoms in the conduction band is remarkable; however, in the surface models the additional contribution of 5*d* states of tungsten in the conduction band and 2*p* states of oxygen in the valence band can be noticed.

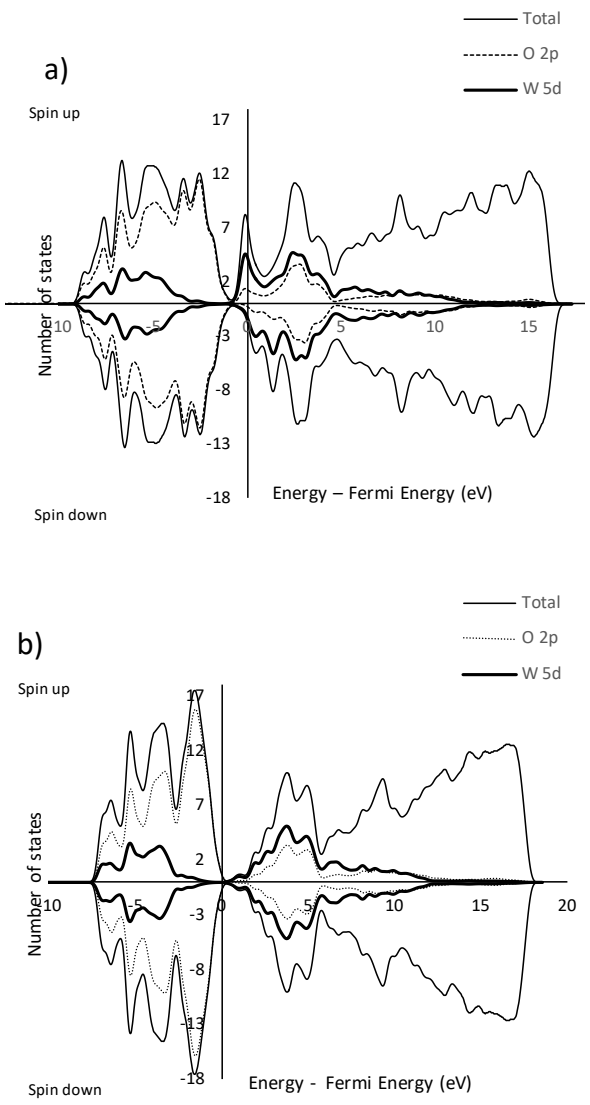

Figure 6. *a). Projected density of states of the tetragonal surfaces (a) model I and (b) model II.*

In both cases the band gap is practically zero, which indicates a migration of the semi-conductor character toward a semimetal character (47). For model I, a shift occurs for the PDOS of electrons with the same energy but different spin.

The PDOS reported in similar studies show a band gap which tends to be small (but not vanishing) for the WO_3 (001) surfaces (Table 6); this feature seems to be peculiar for the tetragonal *P*4/*nmm* WO_3 (50).

Table 6. *Band gap values for the (001) surface of the tetragonal and monoclinic phases of WO_3.*

	XC Functional	WO_3 surface	Band gap (eV)
This work	sp-PP-PBE+vdW	Tetragonal *P4/nmm* (001) Model I	0 (approx)
	sp-PP-PBE+vdW	Tetragonal *P4/nmm* (001) Model II	0 (approx)
Wang *et al.* (44)	B3LYP	ε-Monoclinic (001)	2.71
Lambert-Mauriat *et al.* (48)	PP-PBE	ɤ-Monoclinic (001)	0.30
Jin *et al.* (49)	PP-PW91	ɤ-Monoclinic (001)	0.40

4. Conclusions

In this work, we studied the tetragonal *P*4/*nmm* WO_3 crystal which is of particular interest for the catalytic hydration of ethylene to ethanol. The lattice parameters obtained from periodical DFT calculations turned out to be close to the experimental values previously reported. Also, the calculated band gap was found to be in agreement with the values obtained in similar studies by using other methods for the bulk of the tetragonal *P*4/*nmm* phase or the (001) surface of the monoclinic phase.

Two models of the tetragonal *P*4/*nmm* WO_3 (001) surface were proposed with the aim of studying the structure before and after relaxation and calculating the surface energy. In order to represent the solid surface accurately, a convergence procedure was implemented to obtain suitable values for the number of layers and the vacuum distance between slabs. A number of four layers and a distance of 10 Å were found to be appropriate. A difference of approximately 95 meV/Å^2 between the two

proposed surface models, indicates that surface model II is more stable than surface model I. The surface energy of model II happens to be somewhat larger than the surface energy of the ε-monoclinic phase of WO_3.

The electronic behavior of the slabs (models I and II) looks very interesting, because they lose the semiconductor character of the bulk to acquire a semimetal response. This behavior is in agreement with previous studies, in which a band gap decrease for the surface relative to the bulk has been reported.

5. References

1 Subramani V, Gangwal, SK A review of recent literature to search for an efficient catalytic process for the conversion of syngas to ethanol. Energy & Fuels. 2008; 22(2): 814–39.

2 Llano-Restrepo M, Muñoz-Muñoz YM. Combined chemical and phase equilibrium for the hydration of ethylene to ethanol calculated by means of the Peng-Robinson-Stryjek-Vera equation of state and the Wong-Sandler mixing rules. Fluid Phase Equil. 2011; 307(1): 45-57.

3 Katada N, Iseki Y, Shichi A, Fujita N, Ishino I, Osaki K, *et al*. Production of etanol by vapor phase hydration of ethene over tungsta monolayer catalyst loaded on titania. Appl Catal A General. 2008; 349(1-2): 55-61.

4 Chu W, Echizen T, Kamiya Y, Okuhara T. Gas-phase hydration of ethene over tungstena-zirconia. Appl Catal A General. 2004; 259(2): 199-205.

5 Fougret CM, Hölderich WF. Ethylene hydration over metal phosphates impregnated with phosphoric acid. Appl Catal A General. 2001; 207(1–2): 295–301.

6 Izumi Y. Hydration / hydrolysis by solid acids. Catal. Today. 1997; 33(4): 371-409.

7 Eguchi K, Tokiai T, Arai H. High pressure catalytic hydration of olefins over various proton-exchanged zeolites. Appl Catal. 1987; 34: 275-87.

8 Eguchi K, Tokiai T, Kimura Y, Arai H. High-pressure catalytic hydration of olefins over various proton-exchanged zeolites. Chem Lett. 1986; 15(4): 567-70.

9 Iwamoto M, Tajima M, Kagawa S. Gas-phase direct hydration of ethylene over proton-exchanged zeolite catalysts at atmospheric pres-sure. J Catal. 1986; 101(1): 195–200.

10 Mitsutani A. Future possibilities of recently commercialized acid/base-catalyzed chemical processes. Catal Today. 2002; 73(1–2): 57–63.

11 Lin Y, Tanaka S. Ethanol fermentation from biomass resources: current state and prospects. Appl Microbiol Biotechnol. 2006; 69(6): 627–42.

12 Naik SN, Goud VV, Rout PK, Dalai AK. Production of first and second generation biofuels: a comprehensive review. Renew Sustain Energy Rev. 2010; 14(2): 578–97.

13 Nelson CR, Courter ML. Ethanol by hydration of ethylene. Chem Eng Progr. 1954; 50(10): 526-31.

14 Carle TC, Stewart DM. Synthetic ethanol production. Chem Ind. 1962; 19(5): 830-39.

15 Devon R, Schwartz ML. Ethanol via direct hydration. Chem Eng. 1972; 79(19): 50-51.

16 Millidge AF. Catalytic hydration. In: Miller SA, editor. Ethylene and Its Industrial Derivatives. London: Ernest Benn Limited; 1969, pp. 709-31.

17 Jiang SP. A review of wet impregnation − an alternative method for the fabrication of high performance and nano-structured electrodes of solid oxide fuel cells. Mater Sci Eng A. 2006; 418(1–2): 199–210.

18 Martin C, Solana G, Rives V, Marci G, Palmisano L, Sclafani A. Physico-chemical properties of WO_3/TiO_2 systems employed for 4-nitrophenol photodegradation in aqueous medium. Catal Lett. 1997; 49(3-4): 235–43.

19 Zhang X, Xiu ZM, Li XW. Preparation and characterization of (HAp/SiO_2)/Ti biocomposites. Adv Mat Res. 2011; 217–218: 88–92.

20 Salazar JC. Síntesis y caracterización de catalizadores soportados de TiO2 Y ZrO2 con

tungsteno para su aplicación en la hidratación de etileno a etanol. Tesis pregrado. Departamento de Quimica, Facultad de Ciencias, Universidad del Valle. Cali, Colombia; 2014.

21 Locherer KR, Swainson IP, Salje EKH. Transition to a new tetragonal phase of WO_3 : crystal structure and distortion parameters. J Phys Condens Matter. 1999; 11(21): 4143-56.

22 Nakagawa Y, Tajima N, Hirao K. A theoretical study of catalytic hydration reactions of ethylene. J Comput Chem. 2000; 21(14): 1292–1304.

23 Van Erp TS, Meijer EJ. Proton-assisted ethylene hydration in aqueous solution. Angewandte Chemie Internat Edit. 2004;43(13):1660-62.

24 Scandolo S, Giannozzi P, Cavazzoni C, De Gironcoli S, Pasquarello A., Baroni, S. First-principles codes for computational crystallography in the Quantum-ESPRESSO package. Z Kristallogr. 2005; 220(5–6): 574–79.

25 Giannozzi P, Baroni S, Bonini N, Calandra M, Car R, Cavazzoni C, et al. QUANTUM ESPRESSO: a modular and open-source software project for quantum simulations of materials. J Phys Condens Matter. 2009; 21(39): 395502.

26 Perdew JP, Burke K, Ernzerhof M. Generalized gradient approximation made simple. Phys Rev Lett. 1996; 77(18): 3865–68.

27 Barone V, Casarin M, Forrer D, Pavone M, Sambi M, Vittadini A. Role and effective treatment of dispersive forces in materials: polyethylene and graphite crystals as test cases. J Comput Chem. 2009; 30(6): 934-39.

28 Pack JD, Monkhorst HJ. Special points for Brillouin-zone integrations-a reply. Phys Rev B. 1977; 16(4): 1748–49.

29 Kokalj A. Computer graphics and graphical user interfaces as tools in simulations of matter at the atomic scale. Comput Mat Sci. 2003; 28(2): 155-68.

30 Araujo-Lopez E, Alcala-Varilla L, Seriani N, Montoya JA. TiO_2 anatase's bulk and (001) surface, structural and electronic properties: a DFT study on the importance of Hubbard and van der Waals contributions. Surf Sci. 2016; 653: 187–96.

31 Huang Y, Dong X, Yu Y, Zhang M. The influence of surface oxygen and hydroxyl groups on the dehydrogenation of ethylene, acetic acid and hydrogenated vinyl acetate on pure Pd(100): a DFT study. Appl Surf Sci. 2016; 388(A): 455-60.

32 Morgan BJ, Carrasco J, Teobaldi G. Variation in surface energy and reduction drive of a metal oxide lithium-ion anode with stoichiometry: a DFT study of lithium titanate spinel surfaces. J Mat Chem A. 2016; 4: 17180–92.

33 Dovesi R, Civalleri B, Roetti C, Saunders VR, Orlando R. Ab initio quantum simulation in solid state chemistry. In: Lipkowitz KB, Larter R, Cundan TR., editors. Reviews in Computational Chemistry 21. New York: Wiley; 2005; Chapter 1.

34 Fiorentini V, Methfessel M. Extracting convergent surface energies from slab calculations. J Phys Condens Matter. 1996; 8(36): 6525–29.

35 Chatten R, Chadwick AV, Rougier A, Lindan PJD. The oxygen vacancy in crystal phases of WO_3. J Phys Chem B. 2005; 109(8): 3146–56.

36 Wang F, Di Valentin C, Pacchioni G. Electronic and structural properties of WO_3: a systematic hybrid DFT study. J Phys Chem C. 2011; 115(16): 8345–53.

37 Hjelm A, Granqvist CG, Wills JM. Electronic structure and optical properties of WO_3, $LiWO_3$, NaWO3, and HWO3. Phys Rev B. 1996; 54(4): 2436–45.

38 Perdew JP, Levy M. Physical content of the exact Kohn-Sham orbital energies: band gaps and derivative discontinuities. Phys Rev Lett. 1983; 51(20): 1884–87.

39 Heyd J, Peralta JE, Scuseria GE, Martin RL. Energy band gaps and lattice parameters evaluated with the Heyd-Scuseria-Ernzerhof screened hybrid functional. J Chem Phys. 2005; 123(17): 174101.

40 Alvarez-Quiceno JC, Dalpian GM, Osorio-Guillén JM. A systematic first-principles study of the tungsten trioxide polymorphs. Phys Status Solidi B. 2015; 252(10): 2290–95.

41 Nørskov JK, Holloway S, Lang ND. Microscopic model for the poisoning and promotion of adsorption rates by electronegative and electropositive atoms. Surf Sci. 1984; 137(1): 65–78.

42 Simic-Milosevic V, Heyde M, Lin X, König T, Rust HP, Sterrer M, et al. Charge-induced formation of linear Au clusters on thin MgO films: Scanning tunneling microscopy and density-functional theory study. Phys Rev B. 2008; 78(23): 235429.

43 Sholl D S, Steckel JA. Density Functional Theory: A Practical Introduction, Hoboken: John Wiley & Sons; 2009.

44 Wang F, Di Valentin C, Pacchioni G. DFT study of hydrogen adsorption on the monoclinic WO_3 (001) surface. J Phys Chem C. 2012; 116(19): 10672–79.

45 Perron H, Domain C, Roques J, Drot R, Simoni E, Catalette H. Optimisation of accurate rutile TiO_2 (110), (100), (101) and (001) surface models from periodic DFT calculations. Theor Chem Acc. 2007; 117(4): 565-74.

46 Johnston K, Castell MR, Paxton AT, Finnis MW. $SrTiO_3$ (001) (2x1) reconstructions: first-principles calculations of surface energy and atomic structure compared with scanning tunneling microscopy images. Phys Rev B. 2004; 70: 085415.

47 Burns G. Solid State Physics, New York: Academic Press; 1985.

48 Bandura AV, Sykes DG, Shapovalov V, Troung TN, Kubicki JD, Evarestov RA. Adsorption of water on the TiO2 (rutile) (110) surface: a comparison of periodic and embedded cluster calculations. J Phys Chem B. 2004; 108(23): 7844–53.

49 Lambert-Mauriat C, Olson V, Saadi L, Aguir K. Ab initio study of oxygen point defects on tungsten trioxide surface. Surf Sci. 2012; 606(1–2): 40–45.

50 Jin H, Zhu J, Chen W, Fang Z, Li Y, Zhang Y, et al. Enhanced oxidation reactivity of WO_3 (001) surface through the formation of oxygen radical centers. J Phys Chem C. 2012; 116(8): 5067–75.